

Low-Energy Nuclear Recoil Calibration of XENONnT with a ^{88}YBe Photoneutron Source

E. Aprile ¹ J. Aalbers ² K. Abe ³ S. Ahmed Maouloud ⁴ L. Althueser ⁵ B. Andrieu ⁴ E. Angelino ^{6,7}
 D. Antón Martín ⁸ F. Arneodo ⁹ L. Baudis ¹⁰ M. Bazyk ¹¹ L. Bellagamba ¹² R. Biondi ^{13,*}
 A. Bismark ¹⁰ K. Boese ¹³ A. Brown ¹⁴ G. Bruno ¹¹ R. Budnik ¹⁵ C. Cai ¹⁶ C. Capelli ¹⁰
 J. M. R. Cardoso ¹⁷ A. P. Cimental Chávez ¹⁰ A. P. Colijn ¹⁸ J. Conrad ¹⁹ J. J. Cuenca-García ¹⁰
 V. D’Andrea ^{7,†} L. C. Daniel Garcia ⁴ M. P. Decowski ¹⁸ A. Deisting ²⁰ C. Di Donato ^{21,7}
 P. Di Gangi ¹² S. Diglio ¹¹ K. Eitel ²² S. el Morabit ¹⁸ A. Elykov ²² A. D. Ferella ^{21,7} C. Ferrari ⁷
 H. Fischer ¹⁴ T. Flehmke ¹⁹ M. Flierman ¹⁸ W. Fulgione ^{6,7} C. Fuselli ¹⁸ P. Gaemers ¹⁸
 R. Gaior ⁴ M. Galloway ¹⁰ F. Gao ¹⁶ S. Ghosh ^{23,‡} R. Giacomobono ²⁴ R. Glade-Beucke ¹⁴
 L. Grandi ⁸ J. Grigat ¹⁴ H. Guan ^{23,§} M. Guida ¹³ P. Gyorgy ²⁰ R. Hammann ¹³ A. Higuera ²⁵
 C. Hils ²⁰ L. Hoetsch ¹³ N. F. Hood ²⁶ M. Iacovacci ²⁴ Y. Itow ²⁷ J. Jakob ⁵ F. Joerg ^{13,10}
 Y. Kaminaga ³ M. Kara ²² P. Kavrigin ¹⁵ S. Kazama ²⁷ P. Kharbanda ¹⁸ M. Kobayashi ²⁷
 D. Koke ⁵ A. Kopec ^{26,28} H. Landsman ¹⁵ R. F. Lang ²³ L. Levinson ¹⁵ I. Li ²⁵ S. Li ^{29,¶}
 S. Liang ²⁵ Z. Liang ²⁹ Y.-T. Lin ¹³ S. Lindemann ¹⁴ M. Lindner ¹³ K. Liu ¹⁶ M. Liu ^{1,16}
 J. Loizeau ¹¹ F. Lombardi ²⁰ J. Long ⁸ J. A. M. Lopes ^{17,**} T. Luce ¹⁴ Y. Ma ²⁶ C. Macolino ^{21,7}
 J. Mahlstedt ¹⁹ A. Mancuso ¹² L. Manenti ⁹ F. Marignetti ²⁴ T. Marrodán Undagoitia ¹³
 K. Martens ³ J. Masbou ¹¹ E. Masson ⁴ S. Mastroianni ²⁴ A. Melchiorre ^{21,7} J. Merz ²⁰ M. Messina ⁷
 A. Michael ⁵ K. Miuchi ³⁰ A. Molinario ⁶ S. Moriyama ³ K. Morà ¹ Y. Mosbacher ¹⁵ M. Murra ¹
 J. Müller ¹⁴ K. Ni ²⁶ U. Oberlack ²⁰ B. Paetsch ¹⁵ Y. Pan ⁴ Q. Pellegrini ⁴ R. Peres ¹⁰
 C. Peters ²⁵ J. Pienaar ^{8,15} M. Pierre ¹⁸ G. Plante ¹ T. R. Pollmann ¹⁸ L. Principe ¹¹ J. Qi ²⁶
 J. Qin ^{25,††} D. Ramírez García ¹⁰ M. Rajado ¹⁰ R. Singh ²³ L. Sanchez ²⁵ J. M. F. dos Santos ¹⁷
 I. Sarnoff ⁹ G. Sartorelli ¹² J. Schreiner ¹³ P. Schulte ⁵ H. Schulze Eifing ⁵ M. Schumann ¹⁴
 L. Scotto Lavina ⁴ M. Selvi ¹² F. Semeria ¹² P. Shagin ²⁰ S. Shi ¹ J. Shi ¹⁶ M. Silva ¹⁷ H. Simgen ¹³
 C. Szyszka ²⁰ A. Takeda ³ Y. Takeuchi ³⁰ P.-L. Tan ^{19,1} D. Thers ¹¹ F. Toschi ²² G. Trincherò ⁶
 C. D. Tunnell ²⁵ F. Tönnies ¹⁴ K. Valerius ²² S. Vecchi ³¹ S. Vetter ²² F. I. Villazon Solar ²⁰ G. Volta ¹³
 C. Weinheimer ⁵ M. Weiss ¹⁵ D. Wenz ⁵ C. Wittweg ¹⁰ V. H. S. Wu ²² Y. Xing ¹¹ D. Xu ¹
 Z. Xu ¹ M. Yamashita ³ L. Yang ²⁶ J. Ye ³² L. Yuan ⁸ G. Zavattini ³¹ and M. Zhong ²⁶

(XENON Collaboration)^{††}

¹Physics Department, Columbia University, New York, NY 10027, USA

²Nikhef and the University of Groningen, Van Swinderen Institute, 9747AG Groningen, Netherlands

³Kamioka Observatory, Institute for Cosmic Ray Research, and Kavli Institute for the Physics and Mathematics of the Universe (WPI), University of Tokyo, Higashi-Mozumi, Kamioka, Hida, Gifu 506-1205, Japan

⁴LPNHE, Sorbonne Université, CNRS/IN2P3, 75005 Paris, France

⁵Institut für Kernphysik, University of Münster, 48149 Münster, Germany

⁶INAF-Astrophysical Observatory of Torino, Department of Physics, University of Torino and INFN-Torino, 10125 Torino, Italy

⁷INFN-Laboratori Nazionali del Gran Sasso and Gran Sasso Science Institute, 67100 L’Aquila, Italy

⁸Department of Physics, Enrico Fermi Institute & Kavli Institute for Cosmological Physics, University of Chicago, Chicago, IL 60637, USA

⁹New York University Abu Dhabi - Center for Astro, Particle and Planetary Physics, Abu Dhabi, United Arab Emirates

¹⁰Physik-Institut, University of Zürich, 8057 Zürich, Switzerland

¹¹SUBATECH, IMT Atlantique, CNRS/IN2P3, Nantes Université, Nantes 44307, France

¹²Department of Physics and Astronomy, University of Bologna and INFN-Bologna, 40126 Bologna, Italy

¹³Max-Planck-Institut für Kernphysik, 69117 Heidelberg, Germany

¹⁴Physikalisches Institut, Universität Freiburg, 79104 Freiburg, Germany

¹⁵Department of Particle Physics and Astrophysics, Weizmann Institute of Science, Rehovot 7610001, Israel

¹⁶Department of Physics & Center for High Energy Physics, Tsinghua University, Beijing 100084, P.R. China

¹⁷LIBPhys, Department of Physics, University of Coimbra, 3004-516 Coimbra, Portugal

¹⁸Nikhef and the University of Amsterdam, Science Park, 1098XG Amsterdam, Netherlands

¹⁹Oskar Klein Centre, Department of Physics, Stockholm University, AlbaNova, Stockholm SE-10691, Sweden

²⁰Institut für Physik & Exzellenzcluster PRISMA⁺, Johannes Gutenberg-Universität Mainz, 55099 Mainz, Germany

²¹Department of Physics and Chemistry, University of L’Aquila, 67100 L’Aquila, Italy

²²Institute for Astroparticle Physics, Karlsruhe Institute of Technology, 76021 Karlsruhe, Germany

²³Department of Physics and Astronomy, Purdue University, West Lafayette, IN 47907, USA

²⁴Department of Physics “Ettore Pancini”, University of Napoli and INFN-Napoli, 80126 Napoli, Italy

²⁵Department of Physics and Astronomy, Rice University, Houston, TX 77005, USA

²⁶Department of Physics, University of California San Diego, La Jolla, CA 92093, USA

²⁷Kobayashi-Maskawa Institute for the Origin of Particles and the Universe, and Institute for Space-Earth Environmental Research, Nagoya University, Furo-cho, Chikusa-ku, Nagoya, Aichi 464-8602, Japan

²⁸Department of Physics & Astronomy, Bucknell University, Lewisburg, PA, USA

²⁹Department of Physics, School of Science, Westlake University, Hangzhou 310030, P.R. China

³⁰Department of Physics, Kobe University, Kobe, Hyogo 657-8501, Japan

³¹INFN-Ferrara and Dip. di Fisica e Scienze della Terra, Università di Ferrara, 44122 Ferrara, Italy

³²School of Science and Engineering, The Chinese University of Hong Kong (Shenzhen), Shenzhen, Guangdong, 518172, P.R. China

(Dated: December 17, 2024)

Characterizing low-energy (O(1keV)) nuclear recoils near the detector threshold is one of the major challenges for large direct dark matter detectors. To that end, we have successfully used an Yttrium-Beryllium photoneutron source that emits 152 keV neutrons for the calibration of the light and charge yields of the XENONnT experiment for the first time. After data selection, we accumulated 474 events from 183 hours of exposure with this source. The expected background was 55 ± 12 accidental coincidence events, estimated using a dedicated 152 hour background calibration run with an Yttrium-PVC gamma-only source and data-driven modeling. From these calibrations, we extracted the light yield and charge yield for liquid xenon at our field strength of 23 V/cm between $0.5 \text{ keV}_{\text{NR}}$ and $5.0 \text{ keV}_{\text{NR}}$ (nuclear recoil energy in keV). This calibration is crucial for accurately measuring the solar ^8B neutrino coherent elastic neutrino-nucleus scattering and searching for light dark matter particles with masses below $12 \text{ GeV}/c^2$.

Keywords: Dark Matter, Direct Detection, Xenon, Photoneutron, Calibration

I. INTRODUCTION

The past decade witnessed major improvements in xenon-based dark matter (DM) experiments, bringing us to the verge of entering the “neutrino fog” [1]. ^8B neutrinos from the Sun transfer O(1 keV) energy to the entire nucleus of xenon via a process called coherent elastic neutrino-nucleus scattering (CE ν NS) [2–4]. Recently, the ^8B CE ν NS signal was measured for the first time by the liquid xenon time projection chambers (TPCs) of XENONnT [4] and PandaX [5]. Such a low-energy signal is also characteristic of DM with a mass around $6 \text{ GeV}/c^2$, favored by some light DM models [6–8]. To avoid mismodelling these low-energy nuclear recoil (NR) signatures, it is therefore imperative to properly calibrate the detector response to them. To that end, we conducted an NR calibration of the XENONnT TPC [9] using an external Yttrium-Beryllium (^{88}YBe) photoneutron source. As shown in Fig. 1, neutrons emitted from the ^{88}YBe source have a recoil energy spectrum similar to ^8B CE ν NS, providing the opportunity to characterize this rare process.

XENONnT is one of the leading DM detectors searching for weakly interacting massive particles (WIMPs). It uses a dual-phase TPC filled with liquid xenon, of which

5.9 tonnes constitute its active target [9]. Particle interactions inside the TPC generally produce both scintillation light and ionization electrons in the detector. While the scintillation light generates a prompt signal (S1), the ionization electrons drift upwards and are extracted into a gas phase at the top of the TPC, via applied electric fields. Drift time is the duration required for electrons to be drifted to the liquid-gas interface, with the maximum drift time being 2.2 ms for XENONnT. The extracted electrons produce a secondary scintillation signal (S2) due to their interaction with xenon atoms in the gas phase. Both the S1 and S2 signals are detected in two arrays of photomultiplier tubes (PMTs) placed on the top and bottom of the detector. The drift time between the S1 and S2 signals is used to determine the depth of the interaction which is defined as Z-coordinate, and the scintillation light pattern of the S2 signal as recorded with the top PMT array is used to reconstruct the X and Y coordinates of the interaction. Position and drift time are then used to correct for detector effects and obtain the corrected cS1 and cS2 signal strengths [10]. Furthermore, the ratio between the areas of the S1/S2 signals is crucial for discriminating between NR events and electronic recoil (ER) events. Particles such as neutrons and WIMPs cause NR events by interacting with xenon nuclei, while particles like gamma-rays and electrons cause ER events by interacting with electrons in xenon atoms [11].

This paper describes the calibration of XENONnT using a ^{88}YBe neutron source [12], achieving a low-energy calibration down to approximately $0.5 \text{ keV}_{\text{NR}}$. To understand the background arising from ^{88}Y gamma emissions in the source, additional data was taken with the neutron-emitting beryllium replaced by polyvinyl chloride (PVC) plastic of comparable density and shape.

In the following sections, we will first introduce the de-

* riccardo.biondi@lngs.infn.it

† Also at INFN-Roma Tre, 00146 Roma, Italy

‡ ghosh116@purdue.edu

§ guan81@purdue.edu

¶ lishengchao@westlake.edu.cn

** Also at Coimbra Polytechnic - ISEC, 3030-199 Coimbra, Portugal

†† qinjuehang@rice.edu

‡‡ xenon@lngs.infn.it

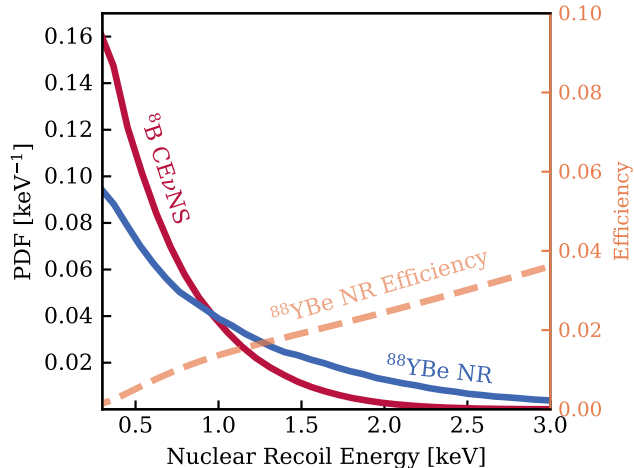


FIG. 1. Comparison of the single-scatter nuclear recoil energy probability density function (PDF) between coherent elastic neutrino-nucleus scattering from solar ${}^8\text{B}$ neutrinos (red) and ${}^{88}\text{YBe}$ neutrons (blue). The similarity and large overlap makes ${}^{88}\text{YBe}$ neutrons an ideal source to calibrate signal yields for the ${}^8\text{B}$ neutrino coherent elastic neutrino-nucleus scattering. In addition, the orange dashed curve denotes the total efficiency for detecting ${}^{88}\text{YBe}$ neutrons in XENONnT.

sign and preparation of the ${}^{88}\text{YBe}$ calibration in Sec. II. Following that, we will discuss calibration operations and explain how to evaluate various backgrounds when selecting data in Sec. III, and finally proceed with fitting and extraction the light and charge yields in Sec. IV.

II. DESIGN OF THE ${}^{88}\text{YBe}$ SOURCE

A. Design Considerations and Challenges

The ${}^{88}\text{YBe}$ photoneutron source produces quasi-monoenergetic 152 keV neutrons via photodisintegration of ${}^9\text{Be}$ by 1.84 MeV γ -rays from ${}^{88}\text{Y}$ decays [12]. One of the key challenges of calibrating with such a source is the low neutron rate due to the small ${}^9\text{Be}(\gamma, n){}^8\text{Be}$ cross-section of 0.65 mb [14], requiring overwhelming γ -ray activity. This low cross section corresponds to a mean free path between photodisintegration interactions of approximately $\rho_{\text{Be}}/m_{\text{Be}}/(0.65 \text{ mb}) \approx 125 \text{ m}$, highlighting how rare such interactions are with centimetre-scale beryllium targets and the comparatively high gamma activity needed to construct a useful calibration source. As meter-scale liquid xenon TPCs have relatively long electron drift times at the millisecond-scale [15, 16], a similarly long event window for matching S1 and S2 signals is required. This results in a high rate of accidental coincidence (AC) events, events resulting from random pairing of S1 and S2 signals. This background will greatly exceed the rate of calibration NR events unless the rate of signals (R_{signals}) in the TPC is kept to be much below

1 kHz. In addition, ER events can contaminate the NR calibration region of interest due to their high rate, even after discrimination between ER and NR events is considered [17]. Therefore, a high atomic number material is needed to effectively block most of the γ -rays from the ${}^{88}\text{Y}$ decays, while minimizing the energy loss of neutrons passing through it.

We mounted the source assembly on the I-belt system of XENONnT [9], and lowered it into the neutron veto detector hosted inside the water Cherenkov muon veto detector [9]. The I-belt subsystem is shown in Fig. 2 (left) in blue, and allows us to control the vertical position of the source and lower it into position beside the cryostat during calibration runs. The size of the assembly houses the ${}^{88}\text{YBe}$ source is restricted to a $(16 \text{ cm})^3$ cube due to mechanical clearances in the I-belt system. This motivates the use of tungsten as the shielding material instead of the more commonly-used lead [12, 18]; while tungsten has a lower atomic number, the density of bulk tungsten is higher, leading to a lower radiation length [19].

Lowering the source assembly past the vacuum flange at the top of the cryostat requires it to be set back with respect to the outer diameter of the cryostat, moving it $\sim 10 \text{ cm}$ away from the cryostat's outer wall. To avoid the broadening of the neutron energy spectrum and the reduction of the neutron flux, we designed and installed an air-filled stainless steel box to displace the water between the TPC and the calibration source with air. The air box was manufactured and fixed to the exterior of the cryostat of XENONnT before commissioning.

B. Optimization of the Source Geometry

In addition to tackling the design challenges mentioned earlier, and to ensure a successful calibration, we optimized the geometry of the source assembly using simulations to improve the signal-to-background ratio. A schematic of the full ${}^{88}\text{YBe}$ source assembly is shown in Fig. 2. The ${}^{88}\text{YBe}$ source is composed of a ${}^{88}\text{Y}$ disc source, containing a $5 \text{ mm} \times 3 \text{ mm}$ (diameter \times height) active element, sandwiched between two identical, cylindrical Be targets.

We used a Geant4 [20] simulation to understand the trade-off between increasing the beryllium target size to increase neutron yields and the corresponding decrease in the amount of tungsten shielding needed to accommodate a larger beryllium target while not exceeding the maximum total physical size of $(16 \text{ cm})^3$, thereby allowing us to improve the signal-to-background ratio. Simulating the ${}^{88}\text{YBe}$ source response in Geant4 is computationally expensive because of the low photodisintegration cross-section. We thus used two separate simulations to estimate the event rate in the XENONnT TPC due to γ -rays and neutrons. First, we estimated the rate of γ -ray-induced neutrons by simulating 1.84 MeV γ -rays from the active element. We then estimated the observed

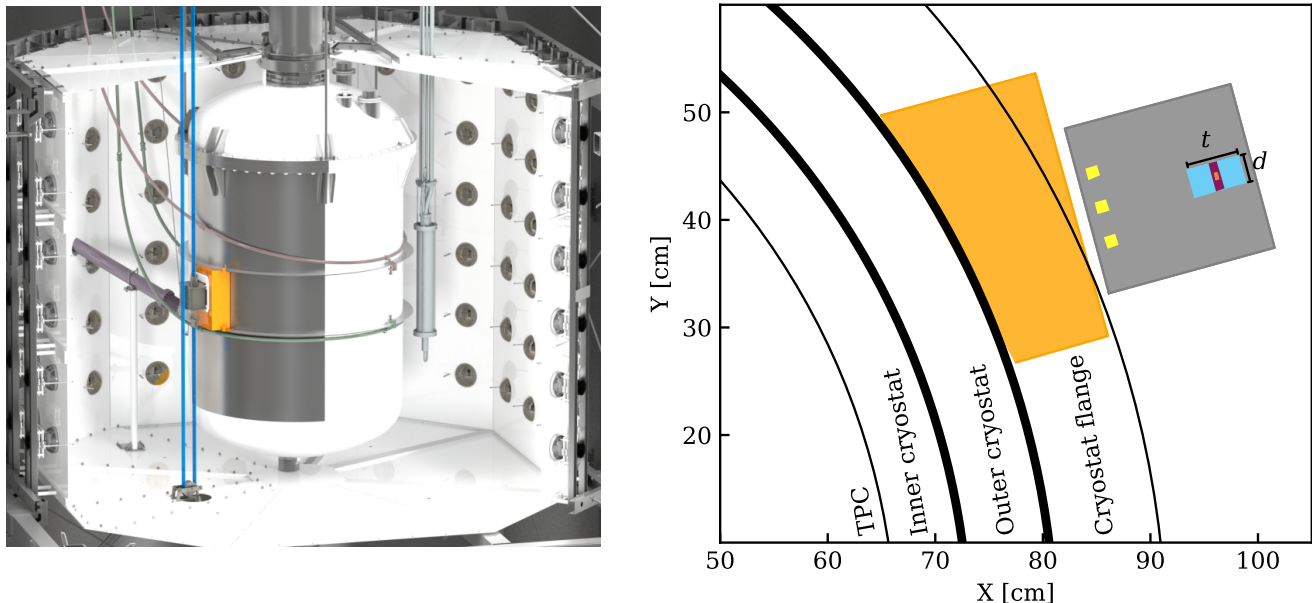


FIG. 2. Left: A CAD rendering of the XENONnT cryostat inside the neutron veto detector (see [9] for more details). Also shown is the I-belt system (blue), along with the tungsten source box (grey) and the water displacement box (orange). Right: The ^{88}YBe source assembly, along with the relevant cryostat parts. In addition to the orange stainless steel air-box, used to displace water between the TPC and the source, and grey tungsten source box, yellow indicates air holes that exist due to the manufacturing process of the tungsten shield, light-blue represents beryllium, purple indicates the acrylic disc that the ^{88}Y source is made of, and the small orange point indicates the ^{88}Y activity. The geometric parameters being optimized are the diameter (d) and thickness (t) of the cavity in the tungsten block containing the beryllium target and ^{88}Y source [13].

neutron rates given the rate of photodisintegration reactions by treating the ^9Be as an isotropic 152 keV neutron source [21], taking light and charge yields, and detector efficiencies [9, 17, 22] into account. Furthermore, S1 and S2 signals generated from multiple scatters of the same primary particle, but close in time and position, may be merged into single S1 and S2 signals. Such effects were also accounted for in the simulation framework.

As these Geant4 simulations considered the neutron and gamma simulations independently without modeling for the photodisintegration reaction that produces neutrons, we need to compute this probability of neutron emission separately to understand the effective exposure time of the neutron simulation. We did this using a Monte Carlo simulation, where we simulated 10^5 γ -rays uniformly from the small cylindrical active element. We then computed the probability of a $^9\text{Be}(\gamma, n)^8\text{Be}$ reaction for each γ -ray based on the trajectory length of the γ -ray in the beryllium target (ℓ) and the number density of beryllium atoms (N_{Be}), as $p_i = \sigma_{\gamma, n} \ell N_{\text{Be}}$. The average probability of $^9\text{Be}(\gamma, n)^8\text{Be}$ reactions per γ -ray is then given by

$$p_{\gamma, n} = \frac{1}{10^5} \sum_i p_i. \quad (1)$$

While only multi-scatter (MS) NR events are considered in the final analysis (see Sections III and IV), during the design stage, we used the ratio of the single-scatter

(SS) NR events to the total TPC event rate as the figure of merit (FOM) for the optimization of the source geometry in order to maximize the signal-to-background ratio of the calibration. These SS events are defined as events with one S1 and one S2 signal in the TPC after combining neighboring signals in space-time, as opposed to multi-scatter events with multiple S1 or S2 signals attributed to the same neutron. The classification of events into SS and MS is dependent on the ability to resolve individual peaks.

While in the Geant4 simulation the beryllium elements are considered to be uniform sources, in reality the gamma flux is higher close to the active element of the ^{88}Y source. To account for this in the computation of the FOM, a per-interaction weight was used to compute the rate of SS NR events in the TPC. This is given by

$$w_i = \frac{\mathcal{N}}{r_i^2}, \quad (2)$$

where \mathcal{N} is a normalizing constant to ensure that the weights sum up to the total number of events, and r_i is the distance between the point of origin of the neutron in the beryllium target and the ^{88}Y source. Since the dimension of the ^{88}Y active element is much smaller than the beryllium target sizes being considered, the ^{88}Y source was approximated as a point source when computing weights. The number of ER or SS NR events is

thus computed as

$$N = \sum_{i \in F} w_i, \quad (3)$$

where F is the set of events being considered, such as SS NR events or ER events.

We finally computed the optimization metric using Eqs. (1) and (2) as

$$\mathcal{S} = \frac{p_{\gamma,n} N_{\text{NRSS}} / S_n}{p_{\gamma,n} N_{\text{ER}} / S_n + N_{\gamma} / S_{\gamma}}, \quad (4)$$

where N_{NRSS} is the number of SS NR events from the Geant4 neutron simulation after weighting computed using (3), N_{ER} is the number of ERs from the Geant4 neutron simulation after weighing computed using (3), N_{γ} is the number of ERs from the gamma simulation, and S_n and S_{γ} is the total number of neutron and gamma primaries from the respective simulations, regardless of whether they formed detectable events in the TPC. This optimization metric can be interpreted as the number of SS NR events expected for each background ER event; a value of $\mathcal{S} = 1$, for example, would mean that we would expect an equal number of SS NR events and background ER events.

Using \mathcal{S} as the FOM, we optimized the dimensions of the cylindrical beryllium targets in two steps: 1) optimizing the thickness while fixing the diameter at $d = 40$ mm, and 2) optimizing the diameter while fixing the thickness at $t = 50$ mm. It can be seen in Fig. 3 that among the considered configurations, the SS NR metric was highest at a thickness of $t = 60$ mm and $d = 25.4$ mm, the diameter of the ^{88}Y disc source. To simplify the source manufacturing, the final thickness of the beryllium target cylinders chosen was 50 mm instead of 60 mm. This decision had minimal impact on the resulting neutron yield.

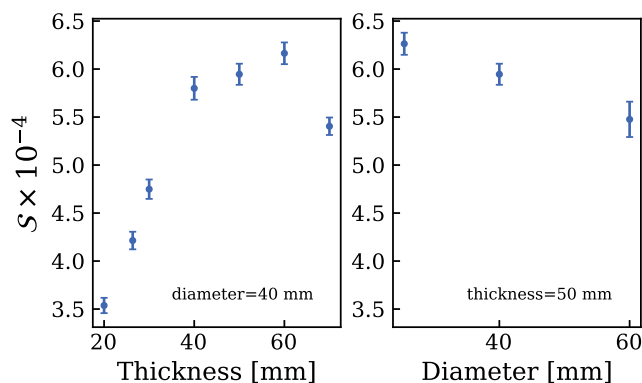


FIG. 3. The variation of \mathcal{S} for thickness and diameter optimization of the beryllium target around the ^{88}Y source. The fixed diameter and thickness values for respective optimizations are also indicated.

Simulations with the chosen geometry gave us a ratio between the SS NR event rate and the total event rate

of $\mathcal{S} = (6.3 \pm 0.1) \times 10^{-4}$, which was higher than all other considered designs shown in Fig. 3. In addition to the above geometry, a stainless steel capsule of 2 mm thickness on all sides, and with a screw-on cap of 3 mm thickness was machined to contain the $50 \text{ mm} \times 25.4 \text{ mm}$ ($t \times d$) neutron source. The full source assembly, including the stainless steel capsule, had dimensions of $55.5 \text{ mm} \times 29.4 \text{ mm}$ ($t \times d$). This resulted in a final 94.5 mm of tungsten between the source capsule and the TPC.

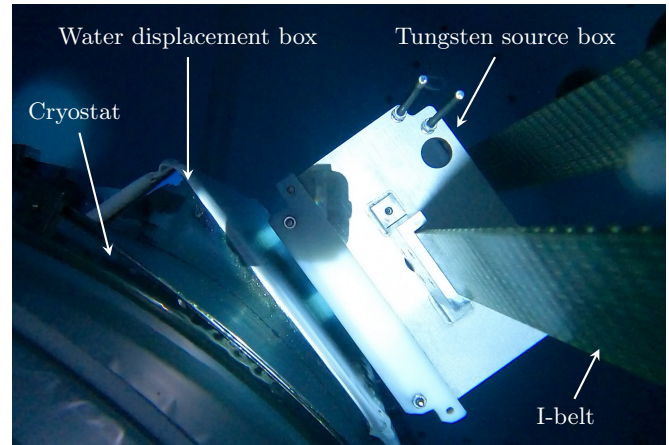


FIG. 4. Image of the I-belt cart containing the tungsten shield and source assembly. This is a top view of the calibration system with a similar orientation to the schematic shown in Fig. 2 right. The cryostat and water displacement box can be seen on the left of this image, whereas the I-belt system can be seen on the right.

III. ^{88}YBE CALIBRATION AND EVENT SELECTION

A. Calibration Operations

^{88}YBe Calibration operations started with the commissioning of the I-belt system, followed by data-taking with the beryllium targets, and finally data-taking with a PVC dummy target replacing the beryllium target. All components that entered the water tank were cleaned with ethanol and deionised water to minimize any impact on the transparency of the water. During commissioning, a waterproof camera was lowered into the water to verify the operation of the I-belt system and that all mechanical components had the expected mechanical clearance. A snapshot from this footage showing the I-belt system and the water displacement box in position can be seen in Fig. 4, showing the full calibration system lowered into the position shown in Fig. 2 (left). After these tests, the tungsten source box was brought back to the water surface, the source assembly containing the targets and the ^{88}Y disc source were inserted, and the combined assembly was lowered back into the calibration position shown in Fig. 2 (left). Starting from September 30th 2022, ^{88}YBe

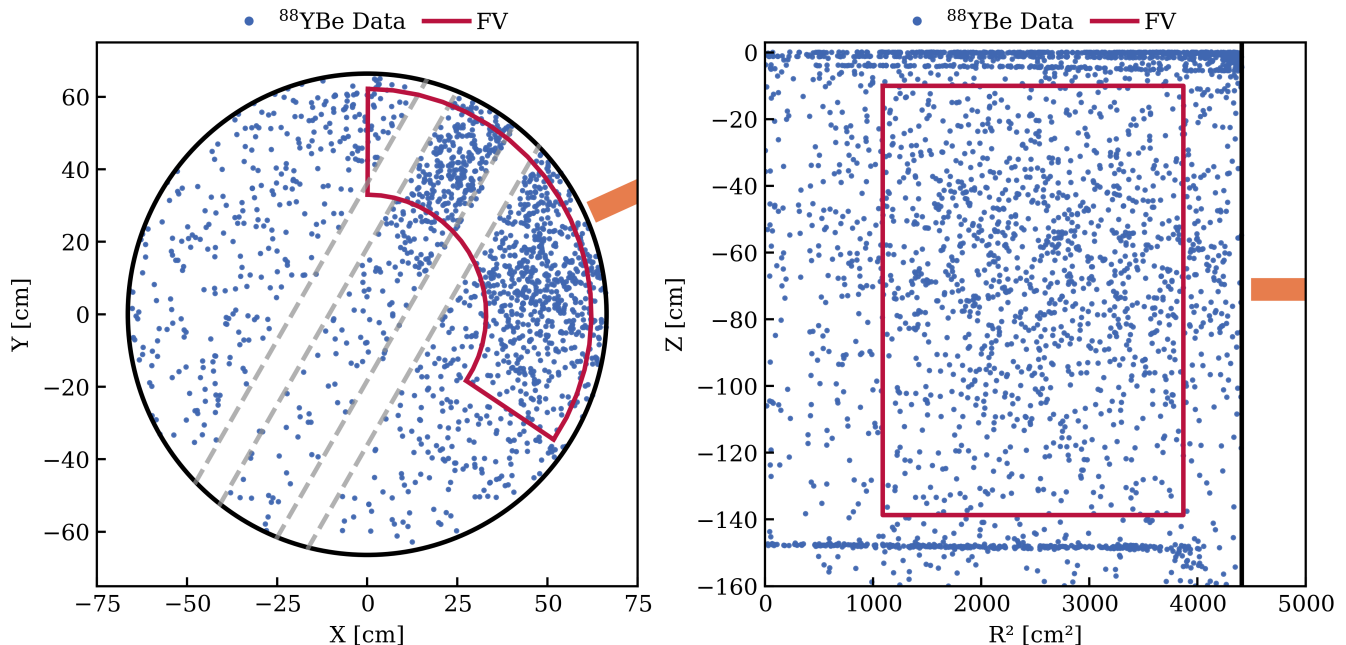


FIG. 5. ^{88}YBe event (blue dots) distribution shown in the XY (left) and R^2Z (right) planes. The events projected onto the XY plane have been selected based on a cut along the z-axis, specifically within the range of $-139 \text{ cm} \lesssim z \lesssim -10 \text{ cm}$. The black solid lines show the position of TPC walls and the orange solid lines indicate the position of the source. The region within the red lines is the employed fiducial volume (FV). Four grey dashed lines indicate two regions near perpendicular wires, which were excluded from the fiducial volume. Clustered events at the top of the R^2Z plane are surface background events, while those at the bottom are cathode events. Events which are outside the fiducial volume and uniformly distributed in the XY plane are mainly residual AC events after removing events in periods with a high rate of delayed electrons and isolated S1 signals.

source data was taken till October 9th, accounting for a total livetime of approximately 183 hours. The ^{88}Y γ -source had an activity of 316 kBq at the start of the calibration. Following this ^{88}YBe calibration, the ^9Be target was replaced by a PVC target with the exact same geometry, and data was taken for an effective livetime of around 152 hours from 10th October 2022.

B. Event Selection

Following the data acquisition, comprehensive analyses were performed to select NR events and subsequently determine the light and charge yields. Due to moderation by the water still remaining between the source and the air box in the neutron veto, the mean kinetic energy of neutrons entering the TPC was lower than the emission energy of 152 keV, with the energies mainly ranging from 10 keV to 100 keV. Since neutrons tend to scatter multiple times in the large volume of liquid xenon and 80% of simulated ^{88}YBe NR events had more than one reconstructed S2, MS neutron NR events were included in the event selection. This was done to maximize statistics and to probe the lowest possible NR energy, even though the geometry of the source had been optimized on the ratio of SS NR events to γ -induced ER background. Selected events had to have at least 2 observed photons and no

more than 10 observed photons in the S1 signal. This upper bound was motivated by the scarcity of NR events with more than 10 observed photons in the S1 signal, as only 7% of NR events were expected to exceed this threshold. Since the mean free time between two scatters for 100 keV neutrons is approximately 30 ns, prompt scintillation photons from different scatters within a MS NR event are merged into one S1. Consequently, in MS NR events, scatters which generate only 1 observed scintillation photon can also be included in this selection. In this way, the energy threshold of this calibration can be further lowered compared to what is obtained from only selecting SS NR events, which were required to have at least 2 observed photons in the S1 signal.

Selecting NR events from the ^{88}YBe source data is challenging, because both γ -rays and neutrons emitted from the ^{88}YBe source interact within the liquid xenon. While neutrons deposit energy through elastic scattering with xenon nuclei, γ -rays primarily interact with xenon atomic electrons via Compton scattering. In this analysis, ^{88}YBe neutron NR events do not overlap with γ -ray ER events, as NR events deposit much lower detectable energies (few keV) and the cS2/cS1 leakage from γ -ray ER events is negligible due to the source design. However, γ -ray ER events with large energy depositions can also induce delayed electrons [23] and isolated S1 signals. Delayed electrons can appear after signal detection, even

beyond the maximum drift time. Possible origins for delayed electrons include electrons captured by impurities in the liquid xenon and released later [23], or electrons trapped at the liquid-gas interface [24]. Isolated S1 signals refer to S1 signals which are not paired with S2 signals within one maximum drift time and may originate from pile-up of PMT afterpulses or PMT dark counts. Isolated S1 signals and delayed electrons can lead to the formation of AC events in two ways, becoming a major background in the low-energy region of NR events. Firstly, the AC events can arise from a random pairing of S2 signals from delayed electrons and isolated S1 signals. Secondly, isolated S1 signals can also form a match with true NR S2 signals, thereby producing AC events. A high rate of delayed-electron S2 signals was observed in the region of $S2 < 120$ PE ($\lesssim 4$ electrons), due to the increased probability of coinciding delayed electrons within the same S2 time window, leading to a significant population of AC events. This motivated the lower S2 area bound of 120PE, while the upper bound of 900 PE was set to minimize ER leakage from γ -ray ER events.

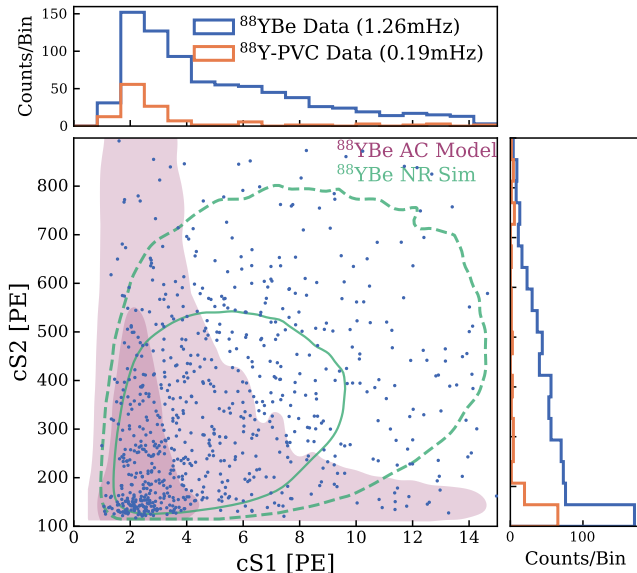


FIG. 6. The distribution of ^{88}YBe events in the $cS1$ - $cS2$ parameter space is presented as blue scatter points. The light (dark) purple region represents the 68% (95%) expected AC events as predicted by the ^{88}YBe AC model. Additionally, the solid (dashed) green contour delineates the 68% (95%) expected NR events. A clustering of events within $cS2 < 200$ PE and $cS1 < 4$ PE shows a substantial population of AC events. 1D projections in the $cS1$ and $cS2$ space are shown for both ^{88}YBe (blue) and $^{88}\text{Y-PVC}$ (orange) calibration data, displayed adjacently. The histogram of the $^{88}\text{Y-PVC}$ data is scaled by a factor of 1.4 to account for the differences in calibration time and the activity of the ^{88}Y source. The ^{88}YBe data includes both AC and NR events, whereas the $^{88}\text{Y-PVC}$ data contains only AC events. Projections for the $^{88}\text{Y-PVC}$ data reveal a significant presence of AC events, particularly in the lowest energy bins, which also suggests a substantial quantity of AC events in the ^{88}YBe data.

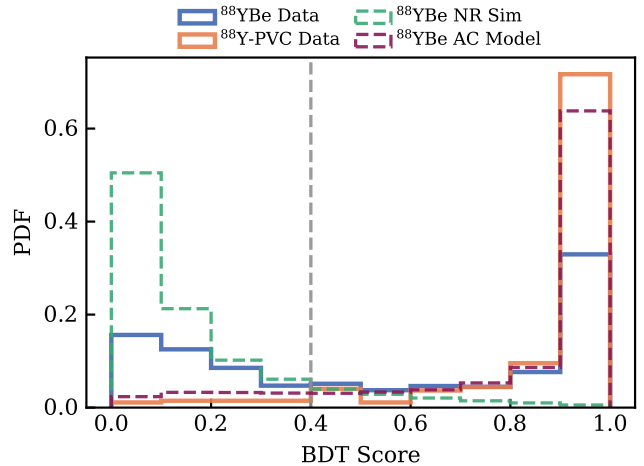


FIG. 7. BDT score distribution, the probability of an event being an AC event, as predicted by the trained BDT classifier. A smaller BDT score indicates a higher probability of an event being NR, while a larger BDT score suggests a higher probability for an event being AC. In $^{88}\text{Y-PVC}$ data, all events are assumed to be AC events while ^{88}YBe data contains both NR and AC events. The BDT score distributions of NR and AC simulation are very distinct, which reflects the satisfactory discrimination power of the trained model. In addition, the grey dashed line represent the cut threshold.

It was observed that delayed electrons and isolated S1 signals exhibit significantly higher rates following large signals, with delayed electrons also showing positional dependence on large preceding S2 signals. To reduce the AC background, we first removed events that were temporally and spatially close to S1 signals larger than 1000 PE or S2 signals larger than 10000 PE, as detailed in [4].

Two additional cuts were developed to further improve the signal-to-background ratio. The first was an optimized fiducial volume cut. As the mean free path for neutrons with these low energies entering the TPC is approximately 10 cm [25, 26] in the liquid xenon, most NR events occur near the TPC wall and are spatially correlated with the source position. However, in the ^{88}YBe data, there was an additional spatially uniform component, similar to that in $^{88}\text{Y-PVC}$ data, which originates from AC events. This component can be reduced using an optimized fiducial volume. The shape of the fiducial volume was determined by a ^{88}YBe NR-only simulation, aiming to encompass 90% of simulated NR events. Additionally, the drift field is distorted [27] near the TPC wall. This leads to the effect that ionization electrons produced from interaction sites close to the wall can be captured by the TPC wall during the drifting to the liquid-gas interface, in turn reducing the size of observed S2 signals originating from regions near the walls. ER events from the ^{88}Y γ -rays were used to study the loss of S2 signal strength near the TPC wall. This analysis resulted in the adoption of an outer radius of 62.2 cm for the fiducial volume, thereby limiting the events adversely affected by this effect to 7%. In addition, two regions near

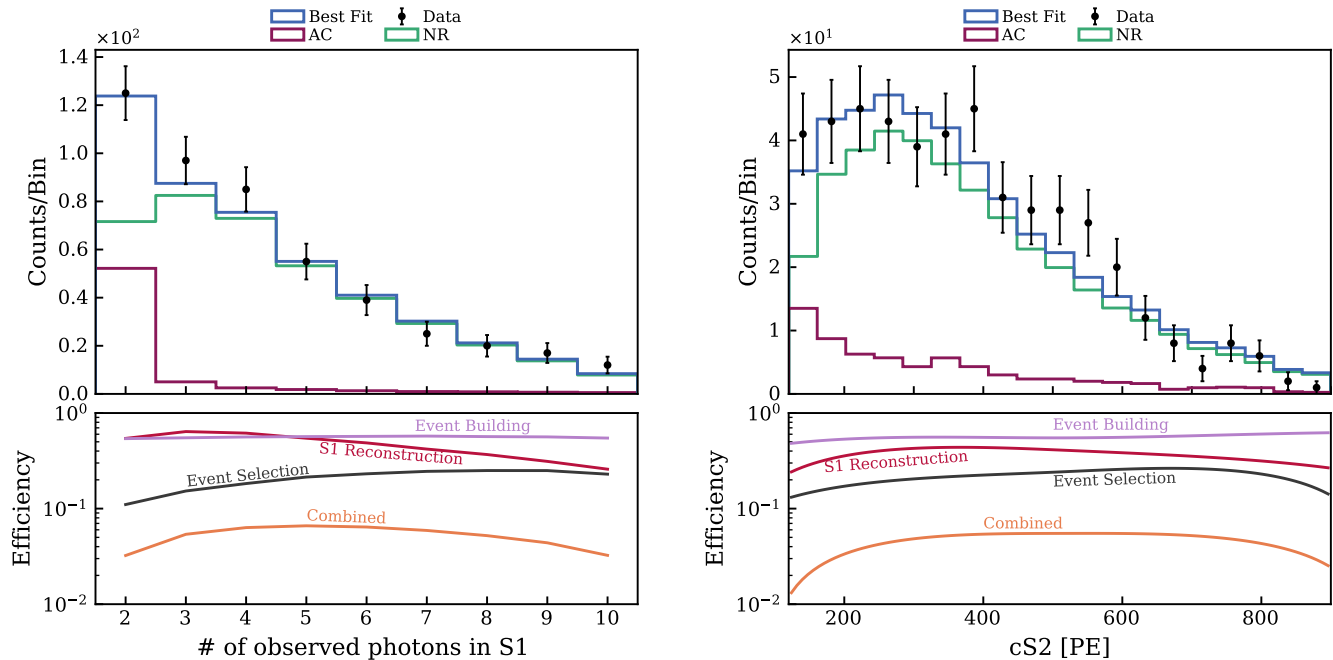


FIG. 8. Top: Comparison of ^{88}YBe best fit simulation (blue) to the ^{88}YBe data (black) in terms of the number of observed photons in S1 (left) and cS2 (right). Both comparisons exhibit excellent agreement between the simulation and the data. Additionally, the individual contributions of NR (green) and AC events (purple) are depicted, providing clear visualization of their respective influences on the overall signal. Bottom: 1D projections of the combined efficiency (orange), which is the product of the S1 reconstruction (red), event building (violet), and event selection efficiency (jet), are shown with respect to the number of observed photons in S1 (left) and cS2 (right)

perpendicular wires on the gate and anode electrodes, which were employed to prevent electrode sagging, were also excluded due to the known difficulty [27] of modeling the pulse shape of S2 signals in these regions. The final shape of the fiducial volume is shown in Fig. 5, where it can be seen that the fiducial volume cut removed a large fraction of AC events.

Events after all above-mentioned cuts are presented in the cS1–cS2 plane in Fig. 6. Comparing the $^{88}\text{Y-PVC}$ and ^{88}YBe data shows that the majority of selected events are NR events. However, the residual events in the $^{88}\text{Y-PVC}$ data indicate a significant presence of AC events in the region of interest (ROI), as the majority of γ -ray ER events have S2 signals larger than 900 PE, while the remaining events in the ROI arise from the random pairing of isolated S1 signals and delayed electrons induced by γ -rays. Thus, a boosted decision tree (BDT) classifier [28] was employed to enhance the discrimination between NR events and AC events, thereby further reducing the AC background. Depending on the separation in space and time among scatters, one or multiple S2 signals can be reconstructed from MS NR events. For events with more than one reconstructed S2 within the event time window, the time, position, and pulse shape information of the two largest S2 signals were used to distinguish between MS and AC events, as the time and position differences among scatters in MS events are cor-

related. NR events with only one reconstructed S2 were difficult to distinguish from AC events and were excluded from the data selection. In the training set for the BDT classifier, the ^{88}YBe NR-only simulation [29] was used as signal. The AC model, used as background, was built by using Axidence [30] to randomly pair isolated S1 signals with S2 signals less than 900 PE in the $^{88}\text{Y-PVC}$ data, as detailed in [4, 11]. To evaluate the performance of the trained model, an independent testing set with one-fourth of the size of the training set was used. After training, the model demonstrated a true positive (signal) rate of 92% and a true negative (background) rate of 86% on the test set, indicating a robust performance with no signs of overfitting. The cut was defined based on the BDT score, which represents the predicted probability of an event being AC, as determined by the trained BDT classifier. The BDT score distribution is shown in Fig. 7. The cut was set to exclude events with an AC score greater than 0.4, effectively rejecting 91% of AC events while retaining 89% of NR events. After applying all cuts, a total of 474 events remained in the ^{88}YBe data. However, a fraction of AC events was still expected to exist among the selected events, particularly those arising from the random pairing of isolated S1 signals and NR S2 signals, which do not exist in the $^{88}\text{Y-PVC}$ data. Therefore, a data-driven AC model [4, 11] based on the ^{88}YBe data was developed to estimate the number of remaining

AC events, resulting in an expectation of (55 ± 12) AC events within the dataset.

IV. FIT AND RESULTS

In order to determine the low-energy NR light and charge yields, quantifying the number of photons and electrons generated per keV of energy deposition in liquid xenon, the selected ^{88}YBe events were fitted by the detector response model using Appletree [31], and the fit region was defined to be the number of observed photons in $S1 \in [2, 10]$ and $cS2 \in [120, 900]$ PE. The detector response model, as detailed in Ref. [11], comprises both the yield model and the detector reconstruction model to generate NR signals. The parameterized Noble Element Simulation Technique (NEST v2) [32] yield model is employed to convert deposited energy into scintillation photons and ionization electrons. Subsequently, the detector reconstruction model transforms these produced photons and electrons into the observed S1 and S2 signals. The drift field dependence of yields in NEST v2 is controlled by two parameters, γ and δ , with the relationship $\varsigma \propto \gamma \mathcal{E}^\delta$, where ς denotes the field dependence and \mathcal{E} represents the drift field strength. However, the ^{88}YBe calibration data was acquired at a single drift field strength of (23 ± 1.5) V/cm. In the fit, δ was fixed at its NEST v2 default value of -0.0533 to avoid degeneracy. We kept all parameters' priors in the yield model, except for δ , uniformly distributed within specific ranges for each parameter. The prior distributions for each parameter in the yield model are detailed in Table I. The data-driven AC model established in the previous section served as background, and a normalization factor was introduced in the fit to scale the AC model, without altering the shape of the AC event spectrum.

TABLE I. Prior and marginal posterior distribution of each parameter in the NR yield model from the ^{88}YBe calibration. The default values of each parameter from NEST v2.3.11 are also shown as a comparison.

Parameter	NEST v2	Prior	Marginal posterior
α	$11.0_{-0.5}^{+2.0}$	[8.5, 21]	$12.1_{-2.3}^{+1.5}$
β	$1.10_{-0.05}^{+0.05}$	[0.85, 1.35]	$0.98_{-0.15}^{+0.09}$
γ	$0.0480_{-0.002}^{+0.002}$	[0.0375, 0.0585]	$0.0447_{-0.0077}^{+0.0052}$
ϵ	$12.6_{-2.9}^{+3.4}$	[0, 29.6]	$13.3_{-5.8}^{+5.2}$
ζ	$0.3_{-0.1}^{+0.1}$	[0, 0.8]	$0.4_{-0.2}^{+0.3}$
η	2_{-1}^{+1}	[-3, 7]	3_{-2}^{+2}
θ	$0.30_{-0.05}^{+0.05}$	[0.05, 0.55]	$0.28_{-0.17}^{+0.16}$
ι	$2.0_{-0.5}^{+0.5}$	[-0.5, 4.5]	$2.2_{-1.6}^{+1.8}$
N_{ex}	0.4	[0, 1]	$0.5_{-0.3}^{+0.3}$
N_i	0.4	[0, 1]	$0.6_{-0.3}^{+0.4}$
ξ	0.50	[0, 1]	$0.48_{-0.34}^{+0.33}$
ω	0.19	[0, 1]	$0.40_{-0.39}^{+0.28}$

Besides the yield model, modeling the detector reconstruction of low-energy NR events is crucial for obtaining reliable yields. Various efficiencies were studied. Firstly, MS NR events have a lower S1 reconstruction efficiency compared to SS NR events. Due to the low speed ($\sim 0.01c$) of ^{88}YBe neutrons and their ability to scatter multiple times in liquid xenon, the time separation between single photons in S1 signals can be larger than that from a SS event. This can lead to incorrect classification of S1 signals as S2 signals or unknown (neither S1 nor S2), thereby reducing the S1 reconstruction efficiency for MS NR events. This effect was more pronounced for MS NR events with large S1 signals, which result from the merging of photons produced by a large number of scatters. Secondly, the high rate of delayed electrons and isolated S1 signals caused by γ -rays can reduce the efficiency of event building, as the event building algorithm may fail when physical S1 or S2 signals are surrounded by too many signals comparable in size. To estimate the event building efficiency for ^{88}YBe NR events, a salting study using Saltax was performed by injecting simulated NR events into ^{88}YBe calibration data [38]. If simulated NR events are introduced into periods with a high rate of delayed electrons and isolated S1 signals, the event building efficiency for these simulated NR events will be reduced. This method allowed for the estimation of the impact of delayed electrons and isolated S1 signals on event building, with a resulting event building efficiency of 56.8%. Thirdly, delayed electrons exhibit strong spatial correlations with γ -ray-induced events, which predominantly occur near the TPC wall. The spatial correlations introduce a spatial dependence in the event selection efficiency, which was evaluated by the study of injecting simulated NR events into the data as well. For instance, the event selection efficiency at $R = 60$ cm was only 25% of that at $R = 40$ cm, thereby illustrating this spatial dependence. The combined efficiency was the product of S1 reconstruction efficiency, event building efficiency and event selection efficiency, as illustrated in Fig. 8. The uncertainty in the combined efficiency was conservatively estimated to be 26%, primarily attributed to the uncertainties associated with the S1 reconstruction efficiency and event selection efficiency.

In total there were 21 parameters in the detector response model, including 12 yield model parameters and 9 Gaussian-constrained detector reconstruction parameters. An affine invariant Markov chain Monte Carlo algorithm [39, 40] was used to sample from this hyperdimensional space to find the best-fit parameters which maximize the posterior. In Fig. 8, the best-fit model shows excellent agreement with the data, yielding a p-value of 0.93 using a binned Poisson χ^2 test [41, 42] defined by Eq. (5). χ^2 is defined to be the log likelihood ratio between the simulation and the data, where \mathcal{L} denotes the likelihood function given by Eq. (6). Here, y and n denote the simulation and the experimental data, respectively. Specifically, y_i and n_i represent the number of events in the i^{th} bin of the simulation and data in the fit region,

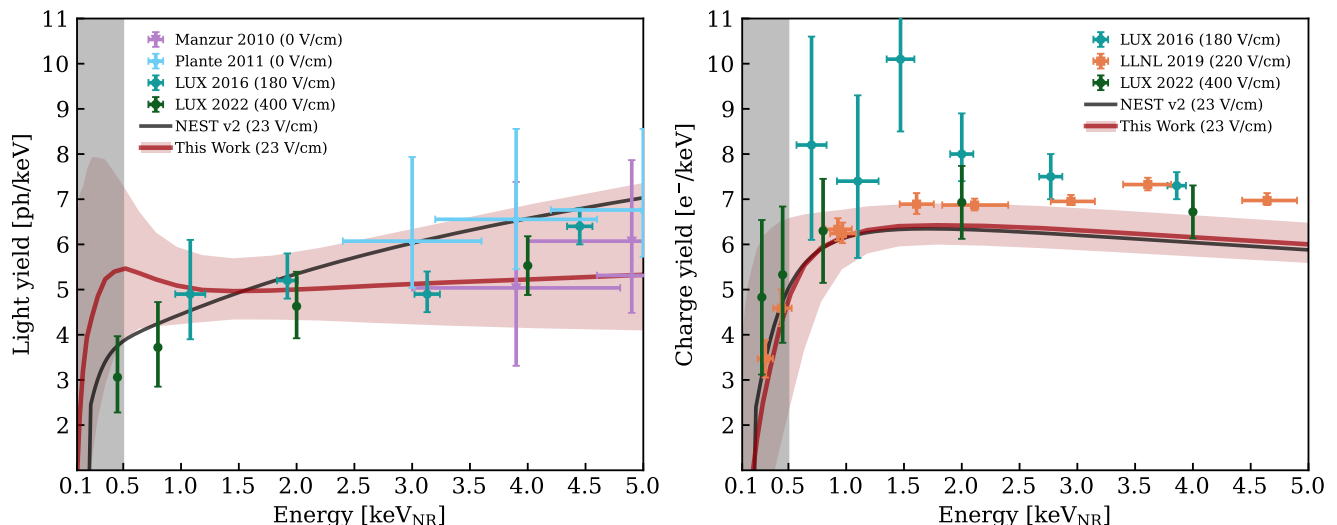


FIG. 9. Light yield (left) and charge yield (right) extracted from the fit to the ^{88}YBe calibration data. The red solid curves represent the nominal yields and red bands show $\pm 1\sigma$ uncertainties of yields. The uncertainty bands are calculated using sampled values of fit parameters in the last 10,000 iterations. The yields from NEST v2.3.11 are shown in black solid curves for comparison. Measurements from other experiments [33–37], taken at different drift field strength, are also shown for comparison. The yields in the grey shaded region are presented solely for completeness, as the lowest energy to which this calibration is sensitive is approximately 0.5 keV_{NR}.

respectively.

$$\chi^2 = -2 \ln \mathcal{L}(y; n) + 2 \ln \mathcal{L}(n; n) \quad (5)$$

$$\mathcal{L}(y; n) = \prod_i \exp(-y_i) \cdot y_i^{n_i} / n_i! \quad (6)$$

Additionally, the best-fit values for all detector reconstruction parameters lie within the $\pm 1\sigma$ uncertainties of the prior estimates. In Fig. 9, the constrained yields from this analysis are compared to the default NEST v2 model. The light yield and charge yields from the fit are in agreement with NEST v2 model within $\pm 1\sigma$ uncertainties. The uncertainties of the fitted yields were estimated using sampled values of fit parameters in the last 10,000 iterations of the fitting process. The constraint on the charge yield is more stringent than the one on light yield because of the low S1 detection efficiency of NRs with energies smaller than 1 keV_{NR}. To determine the lowest energy sensitivity of the calibration, we used the method described in [35]. A range of energy thresholds E_{thr} are applied in the best-fit detector response model, and the resulting $\chi^2(E_{thr})$ is compared to $\chi^2(0)$ of the model without energy threshold to get $\Delta\chi^2 = \chi^2(E_{thr}) - \chi^2(0)$ as shown in Fig. 10. The energy threshold of this analysis is found where $\Delta\chi^2 = 1$. It is found that the lowest observable energy is approximately 0.5 keV_{NR} in the ^{88}YBe calibration.

V. CONCLUSION

The XENONnT collaboration successfully conducted the first calibration of the XENONnT TPC using low-

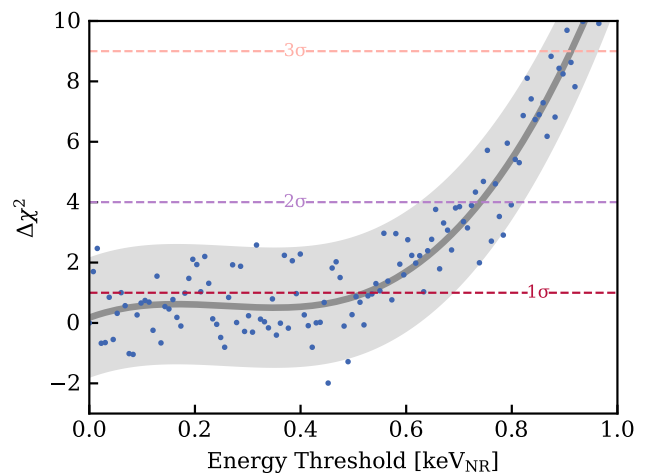


FIG. 10. Estimation of the lowest observable energy in the ^{88}YBe calibration. Each blue point represents $\Delta\chi^2$ between the template generated using the corresponding energy threshold on the x-axis and the best-fit template without any energy threshold. The black curve, along with the grey band, represents a smoothed function obtained using cubic spline interpolation, fitting the blue data points. The energy threshold is set where $\Delta\chi^2 = 1$ and is around 0.5 keV_{NR}.

energy NR events near the detector threshold from a ^{88}YBe photoneutron source. The application of machine learning methods combined with refined simulations enabled us to maximize the number of reconstructed low-energy NR events and address the anal-

ysis challenges posed by the high rate of γ -ray emissions from the source. This calibration enabled us to constrain the light and charge yields in liquid xenon down to $0.5 \text{ keV}_{\text{NR}}$ under a low drift-field condition of 23 V/cm . The constrained yields show no discrepancies with the NEST v2 model and provide vital information for searches involving low-momentum transfer interactions, such as ${}^8\text{B}$ CE ν NS [4, 5], light WIMPs [8], and other rare low-energy NR interactions. Photoneutron sources, such as ${}^{88}\text{YBe}$, offer the advantage of producing quasi-monoenergetic neutrons with relatively low emitted kinetic energies, without the technical complexity of operating a deuterium-deuterium neutron gun. As future underground DM detectors also function as solar neutrino observatories, precise knowledge of the yields near the detector threshold will become even more important for scientific discoveries.

ACKNOWLEDGMENTS

We gratefully acknowledge support from the National Science Foundation, Swiss National Science Foundation, German Ministry for Education and Research, Max Planck Gesellschaft, Deutsche Forschungsgemeinschaft, Helmholtz Association, Dutch Research Council (NWO),

Fundacao para a Ciencia e Tecnologia, Weizmann Institute of Science, Binational Science Foundation, Région des Pays de la Loire, Knut and Alice Wallenberg Foundation, Kavli Foundation, JSPS Kakenhi, JST FOREST Program, and ERAN in Japan, Tsinghua University Initiative Scientific Research Program, DIM-ACAV+ Région Ile-de-France, and Istituto Nazionale di Fisica Nucleare. This project has received funding/support from the European Union’s Horizon 2020 research and innovation program under the Marie Skłodowska-Curie grant agreement No 860881-HIDDeN.

We gratefully acknowledge support for providing computing and data-processing resources of the Open Science Pool and the European Grid Initiative, at the following computing centers: the CNRS/IN2P3 (Lyon - France), the Dutch national e-infrastructure with the support of SURF Cooperative, the Nikhef Data-Processing Facility (Amsterdam - Netherlands), the INFN-CNAF (Bologna - Italy), the San Diego Supercomputer Center (San Diego - USA) and the Enrico Fermi Institute (Chicago - USA). We acknowledge the support of the Research Computing Center (RCC) at The University of Chicago for providing computing resources for data analysis.

We thank the INFN Laboratori Nazionali del Gran Sasso for hosting and supporting the XENON project.

-
- [1] C. A. J. O’Hare, New Definition of the Neutrino Floor for Direct Dark Matter Searches, *Phys. Rev. Lett.* **127**, 251802 (2021), [arXiv:2109.03116 \[hep-ph\]](#).
 - [2] D. Z. Freedman, Coherent effects of a weak neutral current, *Phys. Rev. D* **9**, 1389 (1974).
 - [3] V. B. Kopeliovich and L. L. Frankfurt, Isotopic and chiral structure of neutral current, *JETP Lett.* **19**, 145 (1974).
 - [4] E. Aprile *et al.* (XENON), First Indication of Solar ${}^8\text{B}$ Neutrinos via Coherent Elastic Neutrino-Nucleus Scattering with XENONnT, *Phys. Rev. Lett.* **133**, 191002 (2024), [arXiv:2408.02877 \[nucl-ex\]](#).
 - [5] Z. Bo *et al.* (PandaX), First Indication of Solar B8 Neutrinos through Coherent Elastic Neutrino-Nucleus Scattering in PandaX-4T, *Phys. Rev. Lett.* **133**, 191001 (2024), [arXiv:2407.10892 \[hep-ex\]](#).
 - [6] D. E. Kaplan, M. A. Luty, and K. M. Zurek, Asymmetric Dark Matter, *Phys. Rev. D* **79**, 115016 (2009), [arXiv:0901.4117 \[hep-ph\]](#).
 - [7] S. Tulin and H.-B. Yu, Dark Matter Self-interactions and Small Scale Structure, *Phys. Rept.* **730**, 1 (2018), [arXiv:1705.02358 \[hep-ph\]](#).
 - [8] E. Aprile *et al.* (XENON), First Search for Light Dark Matter in the Neutrino Fog with XENONnT (2024), [arXiv:2409.17868 \[hep-ex\]](#).
 - [9] E. Aprile *et al.* (XENON), The XENONnT dark matter experiment, *Eur. Phys. J. C* **84**, 784 (2024), [arXiv:2402.10446 \[physics.ins-det\]](#).
 - [10] E. Aprile *et al.* (XENON), XENONnT Analysis: Signal Reconstruction, Calibration and Event Selection (2024), [arXiv:2409.08778 \[hep-ex\]](#).
 - [11] E. Aprile *et al.* (XENON), XENONnT WIMP Search: Signal & Background Modeling and Statistical Inference (2024), [arXiv:2406.13638 \[physics.data-an\]](#).
 - [12] J. I. Collar, Applications of an ${}^{88}\text{Y}/\text{Be}$ photo-neutron calibration source to Dark Matter and Neutrino Experiments, *Phys. Rev. Lett.* **110**, 211101 (2013), [arXiv:1303.2686 \[physics.ins-det\]](#).
 - [13] J. Qin, *Computational techniques for the direct detection of dark matter*, *Ph.D. thesis*, Purdue University (2023).
 - [14] A. E. Robinson, Reanalysis of radioisotope measurements of the ${}^9\text{Be}(\gamma, n){}^8\text{Be}$ cross-section, *Phys. Rev. C* **94**, 024613 (2016), [arXiv:1602.05911 \[nucl-ex\]](#).
 - [15] E. Aprile, A. E. Bolotnikov, A. I. Bolozdynya, and T. Doke, Noble gas detectors (Wiley-VCH Verlag, Weinheim, Germany, 2006) pp. 42–45.
 - [16] Hunter, Carter, and Christophorou, Low-energy electron drift and scattering in krypton and xenon., *Physical review. A, General physics* **38** **11**, 5539 (1988).
 - [17] E. Aprile *et al.* (XENON), First Dark Matter Search with Nuclear Recoils from the XENONnT Experiment, *Phys. Rev. Lett.* **131**, 041003 (2023), [arXiv:2303.14729 \[hep-ex\]](#).
 - [18] J. Aalbers *et al.* (LZ), The design, implementation, and performance of the LZ calibration systems, *JINST* **19** (08), P08027, [arXiv:2406.12874 \[physics.ins-det\]](#).
 - [19] R. L. Workman *et al.* (Particle Data Group), Review of Particle Physics, *PTEP* **2022**, 083C01 (2022).
 - [20] S. Agostinelli *et al.* (GEANT4), GEANT4—a simulation toolkit, *Nucl. Instrum. Meth. A* **506**, 250 (2003).
 - [21] B. Hamermesh, M. Hamermesh, and A. Wattenberg, The angular distribution of the photo-neutrons from beryl-

- lium, *Phys. Rev.* **76**, 611 (1949).
- [22] M. Szydagis, J. Balajthy, G. Block, J. Brodsky, J. Cutter, S. Farrell, J. Huang, E. Kozlova, B. Lenardo, A. Manalaysay, D. McKinsey, M. Mooney, J. Mueller, K. Ni, G. Rischbieter, M. Tripathi, C. Tunnell, V. Velan, and Z. Zhao, *Noble element simulation technique* (2022).
- [23] E. Aprile *et al.* (XENON), Emission of single and few electrons in XENON1T and limits on light dark matter, *Phys. Rev. D* **106**, 022001 (2022), [arXiv:2112.12116 \[hep-ex\]](#).
- [24] D. Y. Akimov *et al.*, Observation of delayed electron emission in a two-phase liquid xenon detector, *JINST* **11** (03), C03007.
- [25] N. F. Bell *et al.*, Observing the Migdal effect from nuclear recoils of neutral particles with liquid xenon and argon detectors, *Phys. Rev. D* **105**, 096015 (2022), [arXiv:2112.08514 \[hep-ph\]](#).
- [26] K. Shibata *et al.*, Jendl-4.0: A new library for nuclear science and engineering, *J. nucl. sci. tech* **48**, 1 (2011).
- [27] E. Aprile *et al.* (XENONnT), Design and performance of the field cage for the XENONnT experiment, *Eur. Phys. J. C* **84**, 138 (2024), [arXiv:2309.11996 \[hep-ex\]](#).
- [28] T. Chen and C. Guestrin, XGBoost: A scalable tree boosting system, in *Proceedings of the 22nd ACM SIGKDD International Conference on Knowledge Discovery and Data Mining*, KDD '16 (ACM, New York, NY, USA, 2016) pp. 785–794.
- [29] E. Aprile *et al.* (XENON), Wfsim: The xenon waveform simulator, <https://github.com/XENONnT/WFSim> (2021).
- [30] XENON Collaboration, XENONnT/axidence: strax-based data-driven accidental coincidence background simulation and peak-level salting (2024).
- [31] XENON Collaboration, XENONnT/appletree: A high-performance program simulates and fits response of xenon (2024).
- [32] M. Szydagis *et al.*, A Review of NEST Models, and Their Application to Improvement of Particle Identification in Liquid Xenon Experiments (2022), [arXiv:2211.10726 \[hep-ex\]](#).
- [33] B. Lenardo *et al.*, Measurement of the ionization yield from nuclear recoils in liquid xenon between 0.3 - 6 keV with single-ionization-electron sensitivity (2019), [arXiv:1908.00518 \[physics.ins-det\]](#).
- [34] D. S. Akerib *et al.* (LUX), Low-energy (0.7-74 keV) nuclear recoil calibration of the LUX dark matter experiment using D-D neutron scattering kinematics (2016), [arXiv:1608.05381 \[physics.ins-det\]](#).
- [35] D. S. Akerib *et al.* (LUX), Improved Dark Matter Search Sensitivity Resulting from LUX Low-Energy Nuclear Recoil Calibration (2022), [arXiv:2210.05859 \[physics.ins-det\]](#).
- [36] A. Manzur *et al.*, Scintillation efficiency and ionization yield of liquid xenon for mono-energetic nuclear recoils down to 4 keV, *Phys. Rev. C* **81**, 025808 (2010), [arXiv:0909.1063 \[physics.ins-det\]](#).
- [37] G. Plante *et al.*, New Measurement of the Scintillation Efficiency of Low-Energy Nuclear Recoils in Liquid Xenon, *Phys. Rev. C* **84**, 045805 (2011), [arXiv:1104.2587 \[nucl-ex\]](#).
- [38] XENON Collaboration, XENONnT/saltax (2024).
- [39] D. Foreman-Mackey, D. W. Hogg, D. Lang, and J. Goodman, emcee: the mcmc hammer, *Publ. Astron. Soc. Pac.* **125**, 306 (2013).
- [40] D. Foreman-Mackey *et al.*, emcee v3: A python ensemble sampling toolkit for affine-invariant mcmc, *J. Open Source Softw.* **4**, 1864 (2019).
- [41] S. Baker and R. D. Cousins, Clarification of the Use of Chi Square and Likelihood Functions in Fits to Histograms, *Nucl. Instrum. Meth.* **221**, 437 (1984).
- [42] XENON Collaboration, XENONnT/gofevaluation (2024).